PCCP

Accepted Manuscript

This is an *Accepted Manuscript*, which has been through the Royal Society of Chemistry peer review process and has been accepted for publication.

Accepted Manuscripts are published online shortly after acceptance, before technical editing, formatting and proof reading. Using this free service, authors can make their results available to the community, in citable form, before we publish the edited article. We will replace this *Accepted Manuscript* with the edited and formatted *Advance Article* as soon as it is available.

You can find more information about *Accepted Manuscripts* in the **Information for Authors**.

Please note that technical editing may introduce minor changes to the text and/or graphics, which may alter content. The journal's standard **Terms & Conditions** and the **Ethical guidelines** still apply. In no event shall the Royal Society of Chemistry be held responsible for any errors or omissions in this *Accepted Manuscript* or any consequences arising from the use of any information it contains.

ARTICLE TYPE

Imaging the stereodynamics of methyl iodide photodissociation in the second absorption band: fragment polarization and the interplay between direct and pre dissociation

Marta G. González, Javier D. Rodríguez, Luis Rubio-Lago, and Luis Bañares**

The stereochemistry of methyl iodide photodissociation in the onset of the second absorption B-band has been studied using slice imaging of the $CH_3(v = 0)$ and $I^*(^2P_{1/2})$ photoproducts. The stereodynamical data have been crucial to disentangle the photochemistry of methyl iodide in terms of the competition between direct dissociation and electronic predissociation. The origin of the B-band has been established with high accuracy at 201.11±0.12 nm and a depolarization factor due to parent molecule rotation during predissociation has been found to be 0.29±0.06. Analysis of the semiclassical Dixon's bipolar moments extracted from the $CH_3(v=0)$ sliced images indicates that direct excitation to the A-band $^3A_1$ repulsive state in the vicinity of the origin of the B-band is remarkably enhanced by vibrational coupling between the electronic states involved at the conical intersection through in-plane vibrational motion of the molecule.

1 Introduction

Photoproduct vector correlations constitute a powerful tool to unravel molecular photodissociation mechanisms. The signature that the torques produced by geometrical changes in the excited parent molecule leaves in the photofragments can be traced through the analysis of the spatial direction of the products angular momenta, measured with respect to certain privileged axes. Besides, the anisotropy of the photodissociation process – represented by the β anisotropy parameter – provides direct information about the transition dipole moment of the absorption step. The measurement of β is standardly used to determine the symmetry of any of the states involved in a transition, and in particular, of the excited state which is usually the unknown. On the other hand, deviations from the limiting values for prompt dissociation from perpendicular (β=–1) and parallel (β=2) transitions, arise in dissociation processes mediated by predissociation, isomerization or internal conversion dynamics. In such cases, if the symmetries of the ground and excited states are known, the anisotropy parameter is used to track down the dissociation path.

In this work, we have analyzed the stereodynamics of the methyl iodide photodissociation in the onset of the second absorption B-band in terms of Dixon's semiclassical bipolar moments.[1,2] In 1986 Dixon[3] followed the treatment of Fano and Macek[4] of the interaction of light with arbitrarily aligned and oriented ensembles to describe the photofragment angular momentum polarization in terms of bipolar moments[5] defined in the laboratory frame. According to the formalism, the photofragment angular distribution for a given process can be analytically expressed by a linear multipolar expansion of the spherical harmonics in terms of the bipolar moments.

The number of bipolar moments that can be determined depends on two factors. In first place, on the own nature of the dissociation event. For processes where photofragments are produced with large angular momentum, the high order terms in the multipolar expansion take negligible values. The so called *high-J* limit, where J is the photofragment total angular momentum, corresponds, therefore, to a semiclassical description of the photodissociation process where the bipolar harmonics provide a complete description of the detectable vector correlations.[3] In second place, it depends on the experimental configuration employed. A given photofragment angular distribution depends on the particular laser induced fluorescence (LIF) or resonance enhanced multiphoton ionization (REMPI) transition employed in the detection and on the laser polarization and irradiation geometries. Each combination of those parameters provides a photofragment angular distribution which contains information related to all the significant bipolar moments. A proper choice of laser detection and irradiation configurations would provide a combination of linearly independent equations with the desired set of bipolar moments as solutions. In practice, the possibilities are limited by the experimental set-up. In a molecular beam experiment, the reaction chamber is usually designed for a fixed spatial

Departamento de Química Física, Facultad de Ciencias Químicas, Universidad Complutense de Madrid, 28040 Madrid, Spain. Fax: +34 913944135; Tel: +34 913944228; E-mail: lbanares@ucm.es

configuration of the laser beams; on the other hand, for most polyatomic fragments, the choice of the detection scheme – involving both transition and technique – is scarce. The possible experimental configurations are often reduced to the use of different pump and probe laser polarizations, which for velocity map imaging (VMI) experiments are limited by the Abel inversion constrains[6] or by the use of the forward convolution analysis.[7] Due to the possibility of performing a base-experiment using different pump and probe polarization configurations without the need of any reconstruction method, the ion imaging slicing technique has signified a considerably step forward in the field of stereochemistry.[8]

The lowest energy electronic excitation in methyl iodide corresponds to a $n \rightarrow \sigma^*$ transition, where a nonbonding p electron of iodine is promoted to the lowest energy available antibonding molecular orbital.[9] The spin-orbit (SO) coupling is large due to the presence of the heavy iodine atom and then a SO configuration can be used for the first excited electronic state.[10] Between 220 and 350 nm, the so-called A-band comprises three dipole allowed transitions from the ground state to the $^3Q_1$, $^1Q_1$ and $^3Q_0$ SO (in Mulliken's notation[11]) states.[12] Weak perpendicular transitions to the $^3Q_1$ and $^1Q_1$ states[13] lead to $CH_3(\tilde{X}\ ^2A_2)$ and $I(^2P_{3/2})$ products, while a strong parallel transition to the $^3Q_0$ state produces $CH_3(\tilde{X}\ ^2A_2)$ and $I^*(^2P_{1/2})$ products. A curve crossing between the $^1Q_1$ and $^3Q_0$ states complicates the origin of the $I(^2P_{3/2})$ fragments, since, in principle, they can be produced both adiabatically and nonadiabatically. The A-band includes an additional transition between the ground and the $^3A_1(E)$ state, which lies at higher energies due to the corresponding bonding $\mapsto$ antibonding orbital origin.[14]

The second absorption band in methyl iodide, the B-band, results from the excitation of a nonbonding $5p\pi$ electron of the I atom to a $6s$ molecular Rydberg orbital. The remaining three $5p\pi$ electrons are subject to strong SO coupling, yielding $^2\Pi_{3/2}(^2E_{3/2})$ and $^2\Pi_{1/2}(^2E_{1/2})$ ionic cores in $C_{\infty v}(C_{3v})$ symmetry. These then couple (mainly $J-j$) with the Rydberg electron, and, as a result, lead to states of Δ (E) and Π (E) symmetry with a $^2\Pi_{3/2}(^2E_{3/2})$ ionic core and states (Σ^+, Σ^-) (A_1, A_2) and Π (E) symmetry with a $^2\Pi_{1/2}(^2E_{1/2})$ ionic core. Transitions to those states related with the $^2\Pi_{3/2}(^2E_{3/2})$ ionic core from the $\tilde{X}$ ground state of the molecule, constitute the B-band of methyl iodide, spectrally located in the region from 195 to 205 nm. Given the selection rules (no transitions to either triplets or to states of Ω=2 are allowed from the ground state[9]), the $^1\Pi_1$ state (denoted as state [2] in Refs.[15,16] and as $^3R_1$ in Ref.[14]) dominates absorption from the $\tilde{X}$ ground state, although weak features have been assigned to absorption to the $^1\Pi_2$ state[15,16] (denoted as state [1] in Ref.[15,16] and as $^3R_2$ in Ref.[14]), which lies at slightly lower energies. All those transitions are of E character in C_{3v} symmetry, and are, therefore,

perpendicular.

Contrary to the broad spectral character of the first absorption A-band in CH_3I, purely composed of dissociative valence states, the B-band exhibits clear vibronic structure.[15,16] The considerable spectral broadening observed in the resonances indicate finite lifetimes, which are related to electronic pre-dissociation through surface crossing of the B-band bound $^3R_1$ state with the A–band repulsive $^3A_1(E)$ state.[17,18] Since the $^3A_1(E)$ and $^3Q_0$ states overlap at long C–I distances, the main dissociation channel after excitation to the B-band yields $CH_3(\tilde{X}\ ^2A_2)$ and $I^*(^2P_{1/2})$ products. The production of ground state $I(^2P_{3/2})$ products observed by our group after one photon excitation of the B-band 3^1_0 vibronic transition at 199 nm, has been assigned to an additional predissociation channel produced by the interaction between the bound $^3R_1$ Rydberg state and the repulsive A-band $^1Q_1$ state[19]. Figure 1 shows the details of the potential energy curves that intervene in the excitation/deactivation upon irradiation in this part of the absorption spectrum, according to the *ab initio* calculations of Alekseyev and co-workers[17]. The extreme sensitivity to the vibrational excitation is related to the details of the crossings between the potential energy surfaces and the spatial distributions of the wave functions at each vibrational level. In particular, the *ab initio* calculations show that the $^3A_1(E)$ repulsive state crosses the B-band $^3R_1$ state very close to the equilibrium C–I distance of the latter.

In comparison with product branching ratio and energy partitioning measurements, the stereodynamics of the methyl iodide photodynamics has received considerable less attention. The anisotropy of the process have been characterized with certain detail through the $I^*(^2P_{1/2})$ product[20,21], which cannot show angular momentum alignment and, when using linearly polarized light as in the present case, neither orientation. A direct measurement of the dissociation anisotropy through the methyl product has not been carried out, although qualitative information has been extracted through the β_2 and β_4 anisotropy parameters. Janssen *et al.*[22] demonstrated among others[23,24] that the CH_3 fragment arising from the photodissociation of CH_3I in the A-band has a propensity to inherit the K rotational quantum number of the parent molecule. As a result, rotational alignment correlation is observed. Such effect has been measured for the heavier CD_3I molecule and CD_3 fragment, which possesses rotational resolved transitions.[22] By measuring the dependence of the CD_3 REMPI signal on the angle between the probe and photolysis laser polarizations, the alignment moments $A_0^{(2)}$ and $A_0^{(4)}$ of the CD_3 angular momentum distribution were obtained with respect to the recoil velocity v. Both alignment moments take rather limiting values for most of the rotational transitions studied[22–24]. In the B-band, a possible CH_3 alignment has been proposed to lie at the ground of the analysis of the time-dependent angular dis-

tributions[25,26] and of different rise times found for the methyl fragment in femtosecond time-resolved experiments.[25]

In the present work, the slice imaging technique is used in combination with (2+1) REMPI detection of the $CH_3(v=0)$ and $I^*(^2P_{1/2})$ dissociation products, after excitation of CH_3I between 214 and 199 nm. Four Dixon's bipolar moments have been determined, $\beta_0^2(20)$, $\beta_0^0(22)$, $\beta_0^2(02)$ and $\beta_0^2(22)$, which account, respectively, for the $\mu - v$, $v - J$, $\mu - J$, and $\mu - J - v$ vector correlations, where μ is the transition dipole moment, v the fragment recoil direction, and J the total angular momentum of the detected fragment. The interpretation of the four bipolar moments provides information about the coupling between the CH_3I A- and B-bands, dissociation time scales and details about forces and torques between the separating fragments.

The paper is organized as follows. In Sec. II the experimental approach is presented. Section III describes the experimental results which are discussed in Sec. IV. Finally, Sec. V is dedicated to present the most important conclusions of the work.

2   Experimental

The main characteristics of the experimental setup have been described in detail previously[21,27,28] and thus a brief account of the standard procedure employed in this work will be given here. We have used delayed pulsed extraction slicing[8] in the single field configuration developed by Papadakis and Kitsopoulos and described in detail in Ref.[29] Briefly, the delayed pulsed extraction allows the ion cloud to spread in velocities so that the arrival time of the ion packet at the detector has a width of several hundreds of nanoseconds. By using a narrow detector time gate of a few tens of nanoseconds, we are able to image only the central slice of the ion packet. In the single field configuration, only two electrodes are used and the focusing condition is met when the starting position along the time-of-flight (TOF) axis is at a specific distance from either the repeller or the extractor.

The whole experiment runs at a repetition rate of 10 Hz. A molecular beam is created by expanding a gas mixture of CH_3I in He (10 %, 1 atm backing pressure) into vacuum using a pulsed nozzle (General Valve Series 9, 0.5 mm orifice). The gas pulse passes through a skimmer (Beam Dynamics, Standard Model 2, 0.5 mm diameter orifice) and reaches the ionization chamber, where the molecular beam is intersected at right angles, in the middle of the electrical plates of a TOF mass spectrometer, by the excitation and probe laser pulses, which are focused (f = 25 cm) and counter propagated to each other. To generate excitation radiation between 214 and 199 nm (≈1 mJ/pulse), a sum-frequency mixing nonlinear crystal is used to combine the fundamental and second harmonic radiation of a Nd:YAG (Quanta Ray Pro 230) pumped dye

laser (Sirah Cobra-Stretch). The excitation wavelengths were scanned between 214 and 199 nm and measured by a wavelength meter (Wavemaster Coherent). The photoproducts are resonantly ionized 10 ns later *via* (2+1) REMPI schemes, using a focused probe pulse (≈1.5 mJ/pulse) generated by a Nd:YAG (Quanta Ray Pro 190) pumped frequency doubled dye laser (Sirah Cobra-Stretch). For $CH_3(v = 0)$ detection, the probe laser wavelength was set at 333.45 nm, centered at the Q branch of the $3p_z$ ($^2A_2 \leftarrow^2 A_2$) 0_0^0 transition for a two-photon process. For the detection of $I^*(^2P_{1/2})$ products, the laser was set to 305.57 nm at the $6p^4P_{3/2}$ transition for a two-photon process.[30]

The generated ions are accelerated by the ion optics and pass through a field-free TOF region (45 cm) before hitting the impedance matched microchannel plates (MCPs) (Chevron configuration, 40 mm diameter). The gain of the MCPs can be gated with a high voltage pulse to allow only the ions of interest to be detected. The resulting electron avalanche strikes a phosphor screen (P47), thereby creating the ion image, which is recorded by a charged-coupled device (CCD) camera (SONY 1024 × 768 pixel), controlled using National Instruments (NI) LABVIEW 7.1 and IMAQ VISION software and analyzed with a commercial software (DAVIS). The final image is obtained as the sum of around 40 000 laser shots depending on the quality of the signal. Slice images of the iodine ions are recorded using a 500 ns extraction delay applied on the repeller plate and an effective 10 ns detector gate on the front MCP. The repeller voltage used is 2000 V and the detector voltages are 3.4 kV between back MCP and phosphor screen and 1200 V between back and front MCPs. The front MCP is gated using a pulse of 500 V. Slice images of the methyl ions are recorded using the same conditions, except for a repeller voltage of 5000 V. Ion images are recorded using four laser polarization configurations: X(pump)X(probe), XZ, ZX, and ZZ, where X is perpendicular to the laser propagation axis (Y) and Z is parallel to the molecular beam. The recorded slice images of I^+ or CH_3^+ are quadrant symmetrized prior to extracting the kinetic energy and angular distributions.

Independent velocity-radius calibration of the apparatus is done by measuring resonantly ionized $CH_3(v = 0)$ fragments produced after the photodissociation of CH_3I at 333.45 nm (one color pump-probe experiment) at different repeller potentials, taking advantage of the well known kinetic energy release of the $I(^2P_{3/2})$ yielding channel at this photolysis wavelength[21].

3   Results

3.1   Action spectrum and slice images

A pump-probe experiment has been carried out in which the total $CH_3^+(v = 0)$ ion signal arising from the photodissocia-

tion of CH_3I at different excitation wavelengths in the range 199-214 nm has been measured (product vibrationally state-resolved action spectrum), and it is plotted in Figure 2. The spectrum shows two well defined peaks, corresponding to the B-band 0_0^0 (band origin) and 3_0^1 $^3R_1(E) \leftarrow \tilde{X}(^1A_1)$ vibronic transitions [15,16], seated on a weaker unstructured signal which extends towards longer excitation wavelengths beyond the onset of the B-band. This latter signal arises from direct absorption to the A-band $^3A_1(E)$ repulsive state correlating with $CH_3(v = 0)$ and $I^*(^2P_{1/2})$ fragments (see Figure 1). In this spectrum, there is a salient feature related with the broadening of the base of the main peak corresponding to the 0_0^0 transition that will be discussed later.

Slice images of the $CH_3(v=0)$ and $I^*(^2P_{1/2})$ products for different linear polarization geometries of the pump and probe laser pulses have been measured at excitation wavelengths between 200 and 204 nm (including the B-band origin located at 201.11 nm) indicated in red in Figure 2. $CH_3(v=0)$ sliced images recorded at the XX polarization configuration for the excitation wavelengths 204, 202.5, 201.75, 201.25, 201.11 and 200.25 nm are depicted in Figure 3. For all the excitation wavelengths studied, the $CH_3(v=0)$ images consist of a highly wavelength-dependent anisotropic ring and a low-recoil anisotropic structure. The ring intensity closely follows the profile of the action spectrum shown in Figure 2, increasing as the excitation wavelength is decreased, reaching the maximum at the 0_0^0 resonance of the $^3R_1(E) \leftarrow \tilde{X}(^1A_1)$ transition (at 201.11 nm) and decreasing again as the detuning from the resonance is increased towards shorter wavelengths. Likewise, the evolution of the ring anisotropy seems to follow the pattern defined by the action spectrum: at excitation wavelengths far from the resonant value, the ring shows no signal at the poles of the image, a situation concordant with a pure perpendicular transition; as the excitation wavelength approaches the resonance at either side of the spectral peak centered at 201.11 nm, the ring becomes gradually fuller, and virtually isotropic at the center of the transition (maximum of the 0_0^0 peak in the action spectrum). The low recoil feature, which does not show any particular dependence with excitation wavelength, can be associated to CH_3I^+ ion dissociation [21] and will not be subject of further analysis.

Figure 4 shows the corresponding $I^*(^2P_{1/2})$ XX sliced images recorded at the same excitation wavelengths as those of $CH_3(v=0)$. Interestingly, no signal was found when the detection laser was tuned for resonant multiphoton ionization of $I(^2P_{3/2})$ fragments, which indicates a quantum yield for production of I^* of unity, in agreement with previous works [18,26]. The I^* images depicted in Figure 4 show a single ring, whose intensity and anisotropy follows a similar trend than that observed for the $CH_3(v=0)$ fragment. The ring intensity rises and decreases following the action spectrum profile, and so it does the ring anisotropy, but with a significant difference in

this later case: while the $CH_3(v=0)$ ring becomes isotropic at 201.11 nm − the center of the 0_0^0 transition − the $I^*(^2P_{1/2})$ ring keeps a clear perpendicular intensity distribution at that excitation wavelength.

3.2 Translational energy distributions

Angular integration of the images shown in Figures 3 and 4 yields the translational energy distributions (TEDs) depicted in Figure 5. The energy balance for the photodissociation of CH_3I is given by:

$$E_T[CH_3(v=0)] + E_T(I^*) = h\nu - D_0 + E_i(CH_3I) - E_i[CH_3(v=0)] - E_{SO}[I(^2P_J)] \quad (1)$$

where the first term collects the translational energy of the $CH_3(v=0)$ and $I^*(^2P_{1/2})$ products, ν is the frequency of the excitation laser, D_0=2.41±0.03 eV is the dissociation energy of the $C−I$ bond, [31] $E_{SO}[I(^2P_J)]$ is the spin-orbit (SO) energy of the iodine atom in the ^2P state (for I, E_{SO}=0 and for I^*, E_{SO}=0.943 eV) [31], and $E_i(CH_3I)$ and $E_i[CH_3(v=0)]$ are the internal energies of the parent molecule in the molecular beam and of the $CH_3(v=0)$ fragment, respectively.

It must be noticed that the XX images provide the true shape of the photofragment TEDs because they comprise all the information of the dissociation and detection processes. The $CH_3(v=0)$ and I^* TEDs shown in Figure 5 at the different excitation wavelengths have been normalized to the maximum intensity in each case. Moreover, the KEDs are represented against the available energy fraction channeled into total translational energy (x axis). A value of x=1 provides a reference which allows to interpret the TEDs according to the different energy sources and energy partitioning. Thus, the portion of the TED profiles lying at the left side of the x=1 vertical line shown in the Figure corresponds to signal arising from internally excited fragments. In the case of $CH_3(v=0)$, the width of the profile is related to the rotational content of the $CH_3(v=0)$ fragment, while the width of the $I^*(^2P_{1/2})$ KEDs provides information about the $CH_3(v)$ fragment vibrational distribution. On the other hand, the portion of the TEDs at the right side of the x=1 vertical line corresponds to contributions from photodissociation of vibrationally excited CH_3I, that can be present in the molecular beam in small amounts due to the bad vibrational relaxation in the early part of the supersonic expansion pulse where the experiments are carried out to avoid clusters. [21]

There are relevant features in the TEDs depicted in Figure 5. For excitation wavelengths between 204 nm and 201.75 nm, the internal (mostly vibrational) energy of the CH_3 fragment increases with excitation energy as evidenced in the $I^*(^2P_{1/2})$ TEDs; however, this tendency is reversed for excitation wavelengths between 201.25 nm and 201.11 nm, where a narrow-

ing of the $I^*(^2P_{1/2})$ distributions is observed. At 200.25 nm, the width of the $I^*(^2P_{1/2})$ TED is partially restored to that observed at 201.75 nm. It seems then that there are two clear groups of I* TEDs: those at 204 nm and 201.11 nm, far from and at the 0_0^0 resonance, respectively, and those corresponding to the rest of excitation wavelengths, which are in the near vicinity (to the red and to the blue) of the 0_0^0 resonance at 201.11 nm.

The contribution to the total signal from photodissociation of vibrationally excited CH_3I, clearly evidenced in the $CH_3(v{=}0)$ TEDs, follows a similar pattern to that of the CH_3 internal energy. Between 204 nm and 201.75 nm, the $CH_3(v{=}0)$ TED profiles shift to lower x values and become gradually more symmetric due to an enlargement of the distribution to the right side of the $x{=}1$ reference. The right shoulder visible at 201.75 nm to the right of $x{=}1$ clearly decreases between 201.25 nm and 201.11 nm and increases again at 200.25 nm. As for the I* TEDs, we can distinguish again two groups of $CH_3(v{=}0)$ TEDs depending on the excitation wavelength: one group at 204 nm and 201.11 nm, far from and at the 0_0^0 resonance, respectively, and a second group for those excitation wavelengths in the vicinity of the 0_0^0 resonance.

The non-overlapping regions of the $CH_3(v{=}0)$ and $I^*(^2P_{1/2})$ distributions correspond to vibrationally excited methyl radicals. The $CH_3(v)$ vibrational distribution at the 0_0^0 vibronic transition of the *B*-band has been reported previously[18] and it was concluded that about two thirds of the CH_3 fragments are produced vibrationally excited, primarily in the umbrella v_2 mode. In our case, a rough comparison between the two TEDs at 201.11 nm (see Figure 5) indicates a slightly higher contribution of vibrationless methyl radicals. The remarkable conclusion obtained from the present TEDs is that the vibrational activity of the CH_3 products increases out of the *B*-band 0_0^0 origin in correlation with the participation to photodissociation of vibrationally excited CH_3I. We will discuss later the important repercussions that these results have on the CH_3I photodissociation mechanism in the onset of the *B*-band.

3.3 Angular distributions and vector correlations

For a one-photon dissociation process and $(n{+}m)$ REMPI detection, the photofragment angular distribution can be expressed by an expansion of Legendre polynomials:[3,6,32,33]

$$I(\theta) = \frac{\sigma}{4\pi} \sum_{i=0}^{2n+2} \beta_i P_i(\cos\theta) \qquad (2)$$

where θ is the angle between the photofragment recoil direction and the photolysis laser polarization direction, σ is the absorption cross section, β_i are anisotropy parameters which reflect the dissociation dynamics and the photofragment polarization, P_i are the Legendre polynomials of i-th order and n is the number of photons of the resonant step of the REMPI

process. The $i{=}0$ term corresponds to the population of the studied species, and given that the experimental setup has not been calibrated for total intensities, the whole distribution is normalized to β_0, and the quotient is treated as a normalization fitting parameter. When using linearly polarized pump and probe laser pulses, the experiment is not sensible to photofragment orientation[6] and, therefore, the index i takes only even values.

If no photofragment polarization is expected, Eq. 2 can be truncated at $i{=}2$ and then β_2 coincides with the anisotropy parameter β.[32] Such is the case of the $I^*(^2P_{1/2})$ photofragment arising from photodissociation of CH_3I at the excitation wavelengths studied in this work using linearly polarized light, which with a total angular momentum $J{=}1/2$ cannot show angular polarization (alignment or orientation).[3,6,32,33] Figure 6 shows the $I^*(^2P_{1/2})$ photofragment angular distributions obtained by radial integration of the *XX* sliced images measured at the different excitation wavelengths presented in Figure 4. The angular distributions have been fitted to Eq. 2 truncated at $i{=}2$ and the anisotropy parameters β obtained are indicated in each panel of the Figure.

In the case of the CH_3 fragment, however, the rotational angular momentum is not constrained and can be oriented or aligned with respect to the transition dipole moment μ and the recoil velocity v. Consequently, it is in this case where the $\beta_0^2(20)$, $\beta_0^0(22)$, $\beta_0^2(02)$ and $\beta_0^2(22)$ Dixon's bipolar moments representing the vector correlations of the photodissociation process for this photofragment can be extracted from the $CH_3(v{=}0)$ sliced images recorded at the four polarization configurations of the pump and probe laser beams for each of the excitation wavelengths studied in this work. In Figures 7 and 8, the images measured for the different pump and probe laser polarization geometries at 201.11 nm − which corresponds to the maximum of the 0_0^0 vibronic transition (see above) − and at 200.25 nm − to the blue of the 0_0^0 vibronic transition − are depicted as examples. Similar measurements have been carried out at the other excitation wavelengths studied in this work.

The *XX* images comprise alone all the information regarding the dissociation anisotropy and the orientation and/or alignment of the products. In the *XZ* images, the probe polarization vector lies perpendicular to the detection plane and, therefore, all the information related to the products angular momenta is lost. Similarly, the *ZX* images have lost the information related to the anisotropy of the dissociation process. The *ZZ* images do not contain any dynamical information and are used as a reference to avoid systematic errors, such as detector inhomogeneities. Thus, non-zero β_i^{ZZ} parameters extracted from these *ZZ* images are taken as the instrumental function.

In particular situations, a visual inspection of the images measured at the different polarization geometries provides

valuable beforehand information about the photofragment polarization. In the present case, for instance, the fact that in Figure 8 the XZ and ZZ images do not differ significantly from the XX and ZX images, respectively, indicates that no significant CH_3 polarization is expected for this excitation wavelength (which is out of the maximum of the 0_0^0 transition). On the contrary, the images shown in Figure 7 corresponding to excitation to the center of the 0_0^0 transition indicate that a strong fragment rotational alignment is expected at this excitation wavelength.

All images were radially integrated and the resulting angular distributions were fitted to Eq. 2, resulting in a set of β_i parameters for each of the images measured. Figure 9 depicts the $CH_3(v=0)$ angular distributions obtained from the XX sliced images of Figure 3. The fits obtained using Eq. 2 are shown as red lines. For a $(2+m)$ REMPI detection scheme as the one used in this work for CH_3, three coefficients, β_2, β_4 and β_6 are needed to fit the experimental data. In the present case, however, good fits were obtained in all cases by using β_2 and β_4 (with $\beta_6 \approx 0$), and the values obtained are indicated in each panel of Figure 9.

In this work, we have followed the formalism described by North and co-workers to find the connection between the phenomenological β_i parameters and the Dixon's bipolar moments developed for the case of a $(1+1')$ REMPI detection scheme [1,2]. For a $(1+1')$ REMPI scheme, Eq. 2 is truncated at $i=4$. In addition, since the XX images are the only ones which gather all the dynamical information of the one-photon absorption process, for the XZ and ZX polarization geometries, Eq. 2 is truncated at $i=2$. Accordingly, the total number of β_i parameters is reduced to four, as required to determine the four Dixon's second-order bipolar moments in the high-J limit. For a $(2+1)$ REMPI detection scheme as the one used in the present work, the number of β_i parameters is increased to six. This is so because the β_4^{XZ}, β_6^{XZ} and β_6^{ZX} coefficients are identically zero for a one-photon absorption process independently of the REMPI scheme employed, but, in principle, β_6^{XX} and β_4^{ZX} can take non negligible values. In a previous publication [34], we have proven that the formalism developed by North and co-workers for a $(1+1')$ REMPI detection scheme is constrained only by the number of non-zero β_i parameters and, therefore, in some particular cases, it can be applied to higher order REMPI schemes, as in the present case.

As expected for a polyatomic fragment like CH_3, where high order effects are minimal, the XX images can be fitted using only two parameters (β_2^{XX} and β_4^{XX}) – see above– while a single parameter is needed to fit the ZX images (β_2^{ZX}). This implies that we can take $\beta_6^{XX} \approx 0$ and $\beta_4^{ZX} \approx 0$ and, thus, the number of β_i coefficients is virtually reduced to four, which validates the use of the North and co-workers' $(1+1')$ REMPI formalism [1,2] in the present case. [34] The four measured β_i parameters – β_2^{XX}, β_4^{XX}, β_2^{XZ} and β_2^{ZX} – are, therefore, intro-

duced in Eq. 7 of Refs. [1,2] to calculate the corresponding $\beta_0^2(20)$, $\beta_0^0(22)$, $\beta_0^2(02)$ and $\beta_0^2(22)$ bipolar moments assuming the high-J limit approximation [1]. In the present case, we are probing $CH_3(v=0)$ fragments by $(2+1)$ REMPI through the Q branch of the 0_0^0 transition, which is rotationally congested, and hence the polarization dependence of the measured images permits only the determination of N,K-averaged bipolar moments. The sensitivity factor s_2 ($h^{(2)}$ in Ref. [1]) for detection of the $CH_3(v=0)$ fragment has been calculated previously [34] and its value is 1.88. The results obtained are listed in Table 1.

Figure 10 depicts the anisotropy parameter β as a function of excitation wavelength extracted from the $I^*(^2P_{1/2})$ images and from the $CH_3(v=0)$ $\beta_0^2(20)$ bipolar moments ($\beta \equiv 2\beta_0^2(20)$) superimposed to the $CH_3(v=0)$ action spectrum, while the $\beta_0^0(22)$, $\beta_0^2(02)$ and $\beta_0^2(22)$ bipolar moments are plotted in Figure 11.

4 Discussion

A first and unexpected feature observed in the $CH_3(v=0)$ action spectrum depicted in Figure 2 is the unstructured weak signal which extends from about 214 nm down to the onset of the B-band at about 202 nm. In the gas phase CH_3I absorption spectrum measured by Baronavski and Owrutsky [15], several features associated to vibronic transitions starting from vibrationally excited CH_3I (hot bands) were visible down to 206 nm below the 0_0^0 band origin (the 3_1^0 and 2_1^0 vibronic transitions) [15]. The lack of structure of the weak signal observed here points, however, towards a fast dissociation process after absorption to an electronic state with repulsive character. Such assumption is corroborated by the highly anisotropic ring observed in both the $CH_3(v=0)$ and $I^*(^2P_{1/2})$ sliced images measured at 204 nm (see Figures 3 and 4) at excitation wavelengths well above those corresponding to the onset of the B-band. Moreover, those anisotropic rings are still visible with decreasing intensity up to 214 nm (images not shown). According to the *ab initio* calculations by Alekseyev and co-workers [17,35], excitation to the $^3A_1(E)$ state is the only possible transition from the ground state − that it is dipole-allowed and lies within the Franck-Condon region [14] − between 225 and 200 nm, although it has been assumed to have a negligible contribution to the overall A-band absorption spectrum at excitation wavelengths above 200 nm. [35] In addition, the $^3A_1(E) \leftarrow \tilde{X}(^1A_1)$ transition possesses perpendicular character and correlates with $CH_3(v=0)$ and $I^*(^2P_{1/2})$ fragments, matching the experimental observations reported in this work. In all previous theoretical and experimental studies, the $^3A_1(E)$ state has been associated to the electronic predissociation occurring upon excitation to the bound $^3R_1$ Rydberg state in the three first vibrational levels, [15,17,18,26] $v=0$, $v_3=1$ and $v_2=1$, and only in the femtosecond experiments reported

by Gitzinger *et al.* evidence of a contribution from fast dissociation occurring upon direct absorption to the $^3A_1(E)$ repulsive state at the excitation wavelength corresponding to the weak 3_0^1 vibronic transition has been reported.[26]

The anisotropy of the sliced images shown in Figures 3, 4, 7 and 8 provides valuable information concerning both the absorption and the dissociation steps. Since the $I^*(^2P_{1/2})$ product cannot show angular momentum polarization, the fit of the I^* angular distributions to Eq. 2 provides straightforwardly the anisotropy of the dissociation process. It is quite striking that the β anisotropy parameter is –0.23 only at the very maximum of the $^3R_1 \leftarrow \tilde{X}^1A_1$ 0_0^0 vibronic transition found at 201.11 nm, and decreases abruptly to values of $\beta \approx$ –0.85 at excitation wavelengths in the vicinity (to the red and to the blue) of that maximum.

The symmetry of the CH_3I ground $\tilde{X}(^1A_1)$ and $^3R_1$ electronic states implies that the transition between them must have perpendicular character. The difference between the limiting β=–1 value expected for a perpendicular transition and that observed at the maximum of the 0_0^0 transition at 201.11 nm, β=–0.23, implies a breakdown of the axial recoil limit (ARL). When dissociation occurs on a time scale much faster than the period of rotation of the molecule, the fragments depart along the photodissociating bond in the molecular frame. Such situation corresponds typically to a dissociation through a repulsive potential energy surface, where the excess of energy is channeled preferentially into fragment translational energy. In contrast, a low $\mu - v$ vector correlation characterizes electronic predissociation dynamics, where the lapse of time between excitation and dissociation is governed by the coupling between the bound and dissociative electronic states.[18,26] The effect of the rotational motion of the excited molecule during the photodissociation process on the photofragment angular distribution has been studied widely[36–39], and can be related with the ARL values through a depolarization factor.[39] In the long lifetime limit, the β parameter is reduced to 1/5 of the ARL value,[39] which is in excellent agreement with the present results.

In Figure 10, the β anisotropy parameters obtained from the $\beta_0^2(20)$ bipolar moments extracted from the $CH_3(v=0)$ images are compared to those obtained directly from the I^* images. The β values from both set of data are in good agreement, although the $CH_3(v=0)$ β are, in general, somewhat larger than the I^* β at all excitation wavelengths studied, with the exception of 201.11 nm at the maximum of the 0_0^0 vibronic transition. Several possibilities might lie behind these discrepancies. In first place, it is important to remark that the $I^*(^2P_{1/2})$ product correlates with $CH_3(v)$ fragments with a given vibrational state distribution, mainly in the v_1 (C-H stretching) and v_2 (umbrella) vibrational modes[18], while in the present work only vibrational ground state $CH_3(v=0)$ fragments have been detected. The differences between the two sets of β

anisotropy parameters could be related then with a vibrational state-dependent anisotropy effect, according to which the non-detected vibrationally excited CH_3 fragments would be produced more anisotropically, *i.e.* β values closer to –1, than the detected $CH_3(v=0)$ fragments. At the 0_0^0 absorption maximum at 201.11 nm, however, the opposite effect should be expected since a value of β=–0.34 is obtained for $CH_3(v=0)$ which is more negative than the value of β=–0.23 found for I^*. Considering both the $CH_3(v=0)$ and I^* β values, an averaged depolarization factor of 0.29±0.06 is deduced.

According to these results, we can define a boundary of the spectral region where a pure excitation to the origin (0_0^0 transition) of the *B*-band is produced and electronic predissociation is the dominant photodissociation mechanism (shown as a red shadowed area in Figure 10). Out of this area, the anisotropy parameter β, close to the limiting value for a pure perpendicular transition (β=–1), is consistent with a prompt photodissociation process that can occur only after direct excitation to a purely repulsive potential energy surface, the *A*-band $^3A_1(E)$ state. This result is remarkable since it implies that only in a narrow range of excitation wavelengths in the vicinity of 201.11 nm, the dominant excitation will be to the $v = 0$ vibrational level of the $^3R_1$ Rydberg state comprising the origin of the *B*–band, which will be followed by a predissociation mechanism due to the coupling between the vibrational ground state wave function of the $^3R_1$ Rydberg state and the degenerate continuum of the $^3A_1(E)$ repulsive state. It is only through stereodynamical measurements as those presented in this work that we can reach to such a conclusion.

In a series of experiments carried out previously using femtosecond lasers, the photodissociation time scales after excitation to the 0_0^0 transition of the *B*-band have been determined.[18,26] The lifetime of the predissociative v=0 vibrational state of the $^3R_1$ Rydberg state was found to be 1.52±0.05 ps[18,26]. Relevant to the present work is Figure 2a of Ref. [18] where the evolution of the β parameter extracted from $I^*(^2P_{1/2})$ velocity map ion images measured as a function of the time delay between the pump and probe pulses was presented. The $\beta \approx$ –1 value obtained at about zero time delay evolves towards an asymptotic (long time delays) value of β=–0.5, providing a depolarization factor of 0.5. The β values obtained in the present nanosecond experiments should be compared with the asymptotic β values obtained in the femtosecond experiments, but having in mind the differences between the spectral bandwidths of the laser pulses employed in both experiments. A crucial point is that absorption to the v=0 vibrational state of the bound $^3R_1$ Rydberg state and to the repulsive $^3A_1(E)$ state compete in the excitation wavelength region around the maximum at 201.11 nm. It could be argued that absorption to the bound *B*-band overwhelms the weak absorption to the $^3A_1(E)$ state. On the contrary, the $CH_3(v=0)$ action spectrum depicted in Figure 2 indicates that

absorption to both electronic states lie in a comparable scale, at least for production of vibrationless methyl radicals, which is reflected in the substantial broadening of the 0_0^0 band and the corresponding evolution of β from –0.23 at the maximum to $\approx$–0.85 in its vicinity. The exact weight of each contribution as a function of the excitation wavelength cannot be easily determined, but the anisotropy value given in this work at the very maximum of the 0_0^0 band occurring at 201.11 nm can be considered the true anisotropy for predissociation in the *B*-band. The different bandwidth between the nanosecond and femtosecond laser pulses must account for the differences in the anisotropy values obtained in the present work and those of Ref.[18]. The broad bandwidth inherent to femtosecond laser pulses (a value of 1 nm FWHM is provided in Ref.[18] for the excitation laser – a grey shadowed area has been included in Figure 10 that reflects this bandwidth) implies that the contribution of the $^3A_1(E)$ state to the asymptotic anisotropy in Ref.[18] with a constant β close to the limiting –1 value, must be enough as to lowering the measured average asymptotic β value. Taking into account these considerations, we conclude that the depolarization factor of 0.29±0.06 estimated in this work constitutes a better approximation to the true value than that reported previously from femtosecond experiments[18].

In Figure 11, the $\beta_0^0(22)$, $\beta_0^2(02)$ and $\beta_0^2(22)$ bipolar moments are plotted as a function of the excitation wavelength. Semiclassically, the $\beta_0^2(20)$, $\beta_0^0(22)$ and $\beta_0^2(02)$ bipolar moments can be interpreted as expectation values of the second Legendre polynomial, $\langle P_2(\cos\theta)\rangle$, where θ is the angle between the two relevant vectors in each case, taking each parameter limiting values ranging from –0.5 (if the vectors are orthogonal) to 1 (if the vectors are parallel). Accordingly, dissociation of CH_3I after direct excitation to the $^3A_1(E)$ state results in mild polarization effects, in agreement with the visual analysis discussed in the previous section. The CH_3 rotational angular momentum shows a modest tendency to lie parallel to the recoil direction and perpendicular to the transition dipole moment (small positive $\beta_0^0(22)$ and negative $\beta_0^2(02)$ values, respectively). The triple vector bipolar moment $\beta_0^2(22)$ confirms the former two correlations. In the spectral region corresponding to the maximum of the 0_0^0 transition of the *B*-band − red shadowed area in Figure 11 − the vector correlations are similar to those of the $^3A_1(E)$ state, although the depolarization factor would affect also to these bipolar moments.

Weak vector correlations, reflected on bipolar moments far from the limiting values, are usually associated to vibrational and rotational activity of the parent molecule, which provides both out-of-plane and in-plane motions. Dissociation through a purely repulsive state is faster than the parent molecule rotational period and any photofragment polarization effect that might be observed after photodissociation in a repulsive state must be caused by the initial geometry of the excited photodissociating parent molecule. On the other hand, thermal motion

in the electronic ground state of the parent molecule might lead to a breakdown of the so-called unique recoil direction (URD) approximation, which is an extension of the ARL.[40,41] According to URD, the photofragment recoil v arises from a unique parent molecule geometry. This would be the case for diatomic molecules, where the vibrational motion is produced along the recoil direction. However, in polyatomic molecules the vibrational motion is not in general parallel to the recoil direction, causing the transition dipole moment μ to have a non-single-valued distribution in the molecular frame. The breakdown of the URD implies, consequently, that a certain μ correlates with different *d-v* configurations, where d is the molecule dipole moment. Since the transition probability depends on the scalar product between the photolysis laser polarization direction and the transition dipole moment, for a given μ all the correlating *d-v* configurations are excited with the same probability. According to the results shown in Figure 10, photodissociation of CH_3I in the $^3A_1(E)$ state is characterized by a strong μ-v correlation, which indicates that the transition dipole moment remains perpendicular to the dissociation plane. The weak *v-J* and μ-*J* correlations indicate, in addition, a scrambled CH_3 rotational angular momentum distribution. The combination of both effects suggests a preferential contribution to the absorption process of in-plane in detriment of out-of-plane vibrational modes.

Zero-point vibrational activity of the parent molecule might be enough to break the URD approximation, but in the present case, parent vibrational motion is additionally confirmed by a non-negligible contribution of vibrationally excited CH_3I to the absorption process, as shown in Figure 5. According to the analysis of the CH_3 internal energy carried out in the previous section, the contribution of vibrationally excited parent molecules increases in the vicinity of the 0_0^0 transition, but decreases at the exact resonant transition wavelength. Such result suggests that the in-plane vibrations in the parent molecule act as promoting modes, enhancing the transition probability (Franck-Condon factors) as a result of the vibrational coupling between the $^3A_1$ and $^3R_1$ states at the conical intersection. The fact that conical intersections condition dissociation dynamics beyond the coupling region is well known. In the case of the *A*-band, the vibrational activity of the parent CH_3I enhances the transition probability between 305 and 333.5 nm[21]. The particular promoting mode in that case is the C−I v_3 stretching (see Figure 3 in Ref.[21]) in addition to the v_6 bend and other *e*-symmetry vibrations which enable the C_{3v} to C_s geometry change and, therefore, the $^1Q_1$-$^3Q_0$ conical intersection.[21,28]

At the maximum absorption of the 0_0^0 transition of the *B*-band the situation is different. The large transition dipole moment makes unnecessary any parent molecule vibrational promoting mode and, therefore, the contribution of vibrationally excited CH_3I and, consequently, the vibrational activity of the

CH_3 fragment, decrease. The corresponding bipolar moments differ as well from those obtained from direct excitation to the repulsive $^3A_1(E)$ state. In Figure 11, the $\beta_0^0(22)$, $\beta_0^2(02)$ and $\beta_0^2(22)$ bipolar moments at 201.11 nm corrected by removing the depolarization effect[39] are shown as well. As can be seen, the rotationless corrected bipolar moments are closer to the limiting values, indicating important v-J and μ-J vector correlations produced by torques along the $C-I$ coordinate. The $^3A_1(E)$ repulsive state crosses the vibrationless level, $v=0$, of the $^3R_1$ Rydberg state near the equilibrium geometry, where the 0_0^0 wavefunction shows maximum probability density. Since the transition from the ground state to the $^3R_1$ Rydberg state does not involve a significant change in the CH_3I geometry,[17] no significant available energy is transferred to the internal degrees of freedom of the photofragments. In fact, as described above, CH_3 possesses less internal energy at 201.11 nm than at the other excitation wavelengths studied.

5 CONCLUSIONS

The slice imaging technique has been applied to obtain stereodynamical information for the photodissociation of methyl iodide at different excitation wavelengths in the onset of the second absorption B-band. The stereodynamical analysis of the $CH_3(v=0)$ and $I^*(^2P_{1/2})$ photofragment sliced images in terms of semiclassical Dixon's bipolar moments reveals a strong competition between direct photodissociation from the repulsive A-band $^3A_1(E)$ state and electronic predissociation from the vibrationless level of the B-band $^3R_1$ Rydberg state. The stereodynamical data provide a precise value for the origin of the 0_0^0 transition of the B-band at 201.11±0.12 nm and a depolarization factor due to parent molecule rotation of 0.29±0.06. The analysis of the Dixon's bipolar moments $\beta_0^0(22)$, $\beta_0^2(02)$ and $\beta_0^2(22)$ provide detailed information on the absorption process and the dissociation step. A remarkable enhancement of absorption to the A-band $^3A_1(E)$ state favoring prompt dissociation is provided by vibrational coupling with the bound $^3R_1$ Rydberg state.

Acknowledgements

References

1 M. P. Grubb, M. L. Warter, C. D. Freeman, N. A. West, K. M. Usakoski, K. M. Johnson, J. A. Bartz and S. W. North, *J. Chem. Phys.*, 2011, **135**, 094201.
2 M. P. Grubb, M. L. Warter, C. D. Freeman, N. A. West, K. M. Usakoski, K. M. Johnson, J. A. Bartz and S. W. North, *J. Chem. Phys.*, 2012, **136**, 219901.
3 R. N. Dixon, *J. Chem. Phys.*, 1986, **85**, 1866.
4 U. Fano and J. H. Macek, *Rev. Mod. Phys.*, 1973, **45**, 553.
5 D. A. Case, G. M. McClelland and D. R. Herschbach, *Mol. Phys.*, 1978, **35**, 541.
6 T. P. Rakitzis, *Chem. Phys. Lett.*, 2001, **342**, 121.
7 V. K. Nestorov, R. D. Hinchliffe, R. Uberna, J. I. Cline, K. T. Lorenz and D. W. Chandler, *J. Chem. Phys.*, 2001, **115**, 7881.
8 C. R. Gebhardt, T. P. Rakitzis, P. C. Samartzis, V. Ladopoulos and T. N. Kitsopoulos, *Rev. Sci. Instrum.*, 2001, **72**, 3848.
9 R. S. Mulliken and E. Teller, *Phys. Rev.*, 1942, **61**, 283.
10 G. Herzberg, *G. Herzberg*, 1996, vol. Molecular Spectra and Molecular Structure III. Electronic Spectra and Electronic Structure of Polyatomic molecules.
11 R. S. Mulliken, *J. Chem. Phys.*, 1940, **8**, 382.
12 A. Gedanken and M. D. Rowe, *Chem. Phys. Lett.*, 1975, **34**, 39.
13 R. S. Mulliken, *Phys. Rev.*, 1936, **50**, 1017.
14 A. B. Alekseyev, H.-P. Liebermann, R. J. Buenker and S. N. Yurchenko, *J. Chem. Phys.*, 2007, **126**, 234102.
15 A. P. Baronavski and J. C. Owrutsky, *J. Chem. Phys.*, 1998, **108**, 3445.
16 M. R. Dobber, W. J. Buma and C. A. de Lange., *J. Chem. Phys.*, 1993, **99**, 836.
17 A. B. Alekseyev, H.-P. Liebermann and R. J. Buenker, *J. Chem. Phys.*, 2011, **134**, 044303.
18 G. Gitzinger, M. E. Corrales, V. Loriot, G. A. Amaral, R. de Nalda and L. Bañares, *J. Chem. Phys.*, 2010, **132**, 234313.
19 M. G. González, J. A. Rodríguez, L. Rubio-Lago and L. Bañares, *J. Chem. Phys.*, 2011, **135**, 021102.
20 A. T. Eppink and D. H. Parker, *Rev. Sci. Instrum.*, 1997, **68**, 3477.
21 L. Rubio-Lago, A. García-Vela, A. Arregui, G. A. Amaral and L. Bañares, *J. Chem. Phys.*, 2009, **131**, 174309.
22 M. H. M. Janssen, D. H. Parker, G. O. Sitz, S. Stolte and D. W. Chandler, *J. Phys. Chem.*, 1991, **95**, 8007.
23 D. Y. Kim, N. Brandstater, L. Pipes, T. Garner and D. Baugh, *J. Phys. Chem.*, 1995, **99**, 4364.
24 P. J. Pisano and J. I. Cline, *J. Chem. Phys.*, 2000, **112**, 6190.
25 N. Thire, R. Cireasa, D. Staedter, V. Blanchet and S. T. Pratt, *Phys. Chem. Chem. Phys.*, 2011, **13**, 18485.
26 G. Gitzinger, M. E. Corrales, V. Loriot, R. de Nalda and L. Bañares, *J. Chem. Phys.*, 2012, **136**, 074303.
27 L. Rubio-Lago, J. A. Rodríguez, A. García-Vela, M. G. González, G. A. Amaral and L. Bañares, *Phys. Chem. Chem. Phys.*, 2011, **13**, 8186.
28 M. G. González, J. A. Rodríguez, L. Rubio-Lago, A. García-Vela and L. Bañares, *Phys. Chem. Chem. Phys.*, 2011, **13**, 16404.
29 V. Papadakis and T. N. Kitsopoulos, *Rev. Sci. Instrum.*, 2006, **77**, 083101.
30 Y.-J. Jung, Y. S. Kim, W. K. Kanga and K.-H. Jung, *J. Chem. Phys.*, 1997, **107**, 7187.
31 A. T. J. B. Eppink and D. H. Parker, *J. Chem. Phys.*, 1998, **109**, 4758.
32 R. N. Zare, *R. N. Zare*, 1998, vol. Angular Momentum: Understanding Spatial Aspects in Chemistry and Physics.
33 T. P. Rakitzis and R. N. Zare, *J. Chem. Phys.*, 1999, **110**, 3341.
34 J. A. Rodríguez, M. G. González, L. Rubio-Lago, L. Bañares, P. Samartzis and T. N. Kitsopoulos, *J. Chem. Phys.*, 2013, **117**, 8175.
35 A. B. Alekseyev, H.-P. Liebermann and R. J. Buenker, *J. Chem. Phys.*, 2007, **126**, 234103.

36 C. Jonah, *J. Chem. Phys.*, 1971, **55**, 1915.

37 S. Yang and R. Bersohn, *J. Chem. Phys.*, 1974, **61**, 4400.

38 V. V. Kuznetsov and O. S. Vasyutinskii, *J. Chem. Phys.*, 2005, **123**, 034307.

39 L. Bougas and T. P. Rakitzis, *J. Chem. Phys.*, 2011, **13**, 8526.

40 T. P. Rakitzis and A. J. Alexander, *J. Chem. Phys.*, 2010, **132**, 224310.

41 T. P. Rakitzis, *Phys. Chem. Chem. Phys.*, 2010, **133**, 204301.

Tables

Table 1 Dixon's second-order bipolar moments extracted from the analysis of the $CH_3(v=0)$ sliced images at the different excitation wavelengths studied in this work.

λ_{exc} / nm	$\beta_0^2(20)$	$\beta_0^0(22)$	$\beta_0^2(02)$	$\beta_0^2(22)$
201.75	-0.39 ± 0.02	0.18 ± 0.03	-0.05 ± 0.07	0.09 ± 0.02
201.50	-0.41 ± 0.04	0.12 ± 0.02	-0.07 ± 0.05	0.04 ± 0.03
201.25	-0.22 ± 0.02	0.17 ± 0.04	-0.13 ± 0.04	-0.01 ± 0.01
201.11	-0.17 ± 0.04	0.11 ± 0.06	-0.08 ± 0.06	-0.07 ± 0.05
201.00	-0.38 ± 0.02	0.15 ± 0.02	-0.17 ± 0.04	-0.05 ± 0.05
200.90	-0.43 ± 0.01	0.20 ± 0.09	-0.23 ± 0.06	-0.08 ± 0.06
200.75	-0.43 ± 0.01	0.18 ± 0.02	-0.22 ± 0.03	-0.03 ± 0.03
200.25	-0.48 ± 0.05	0.18 ± 0.02	-0.05 ± 0.07	-0.09 ± 0.02

Figures
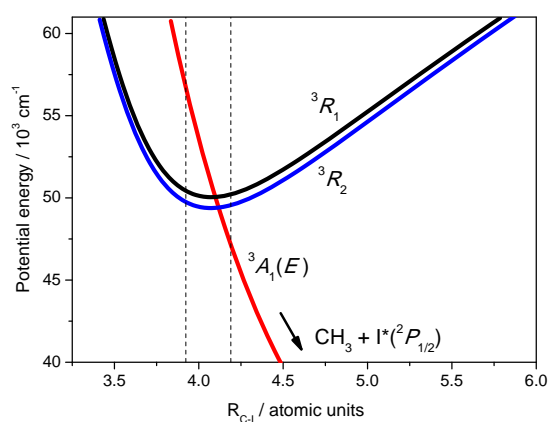
Fig. 1 *Ab initio* potential energy curves involved in the photodissociation of CH_3I in the second absorption *B*-band. Adapted from Ref. [17]. See the text for details about the electronic states involved.
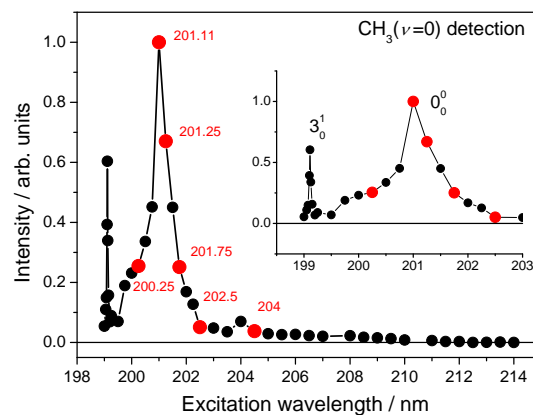
Fig. 2 $CH_3(v=0)$ fragment action spectrum from CH_3I photodissociation at the onset of the second absorption *B*-band. The action spectrum covers the origin of the *B*-band (0_0^0 vibronic transition) and the 3_0^1 vibronic band. Excitation wavelengths at which $CH_3(v=0)$ and $I^*(^2P_{1/2})$ images have been measured are shown with red circles.
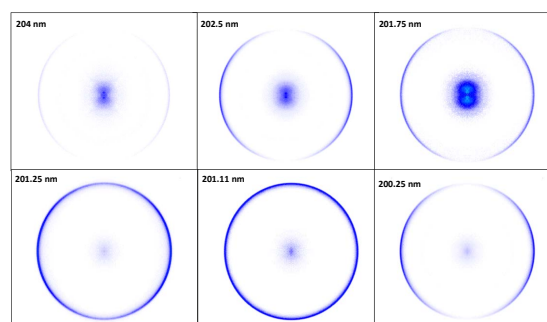
Fig. 3 Slice images (*XX* polarization configuration) of the $CH_3(v=0)$ photofragment arising from CH_3I photodissociation at different excitation wavelengths covering the 200-204 nm range around the onset of the *B*-band.
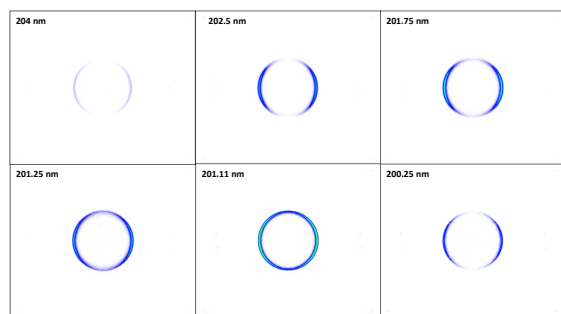
Fig. 4 Slice images (*XX* polarization configuration) of the $I^*(^2P_{1/2})$ photofragment arising from CH_3I photodissociation at different excitation wavelengths covering the 200-204 nm range around the onset of the *B*-band.
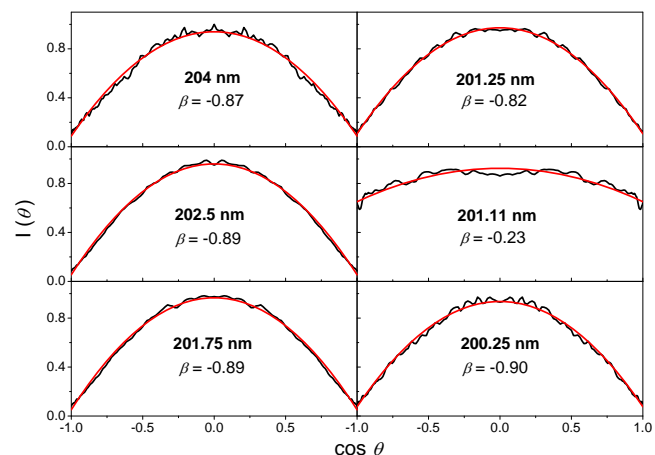
Fig. 6 $I^*(^2P_{1/2})$ angular distributions at the different excitation wavelengths obtained by radial integration of the images shown in Figure 4. The red curves represent the fit of the experimental data to Eq. 2. The β anisotropy parameters obtained from the fit are indicated in each panel.
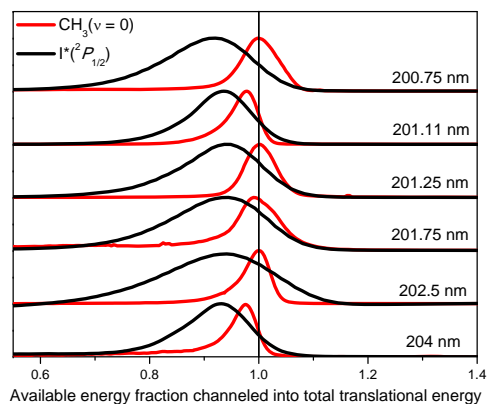
Fig. 5 $CH_3(v=0)$ (red) and $I^*(^2P_{1/2})$ (black) translational energy distributions represented as a function of the available energy fraction appearing as total translational energy at different excitation wavelengths obtained by integration of the corresponding slice images shown in Figs. 3 and 4. En each case, the $CH_3(v=0)$ and $I^*(^2P_{1/2})$ distributions are normalized to have the same intensity at the maximum.
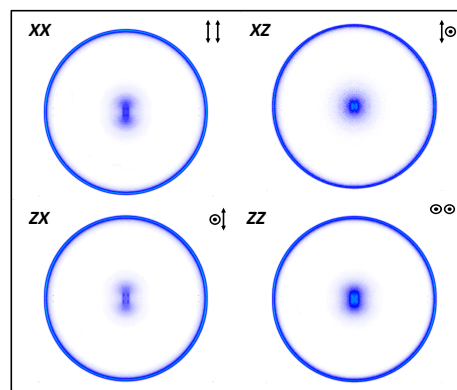
Fig. 7 Sliced images corresponding to $CH_3(v=0)$ fragments produced in the photodissociation of CH_3I at 201.11 nm measured at the different pump-probe polarization configurations *XX*, *XZ*, *ZX* and *ZZ* (see the text for details). The pump and probe laser linear polarizations are indicated at the top right side of each image. An arrow represents perpendicular polarization and a circle with central dot represents parallel polarization to the *Z* axis, which is parallel to the molecular beam.
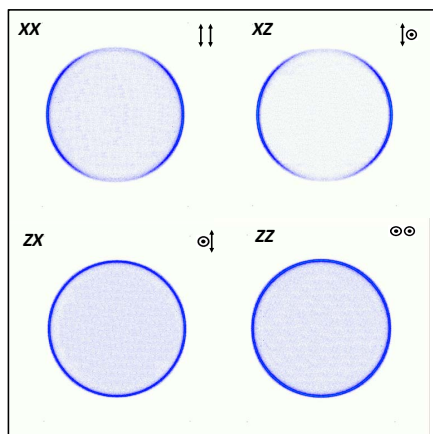
Fig. 8 Same as Figure 7, but for the excitation wavelength 200.25 nm.
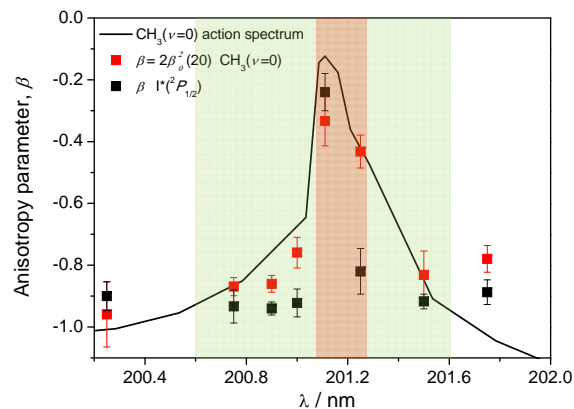
Fig. 10 Variation of the dissociation anisotropy β extracted from the $I^*(^2P_{1/2})$ images (black squares) and from the $CH_3(v=0)$ $\beta_0^2(20)$ bipolar moments (red squares), superimposed to the $CH_3(v=0)$ action spectrum (black line). The vertical scale corresponds to the anisotropy parameter, while the action spectrum has been rescaled in arbitrary units to fit in the graph.
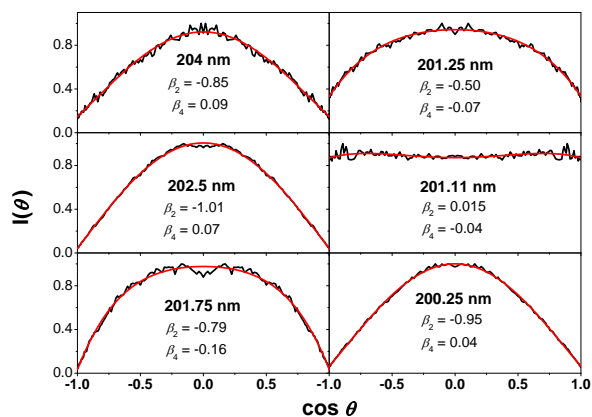
Fig. 9 $CH_3(v=0)$ angular distributions at the different excitation wavelengths obtained by radial integration of the *XX* images shown in Figure 3. The red curves represent the fit of the experimental data to Eq. 2. The β_2 and β_4 anisotropy parameters obtained from the fit are indicated in each panel.
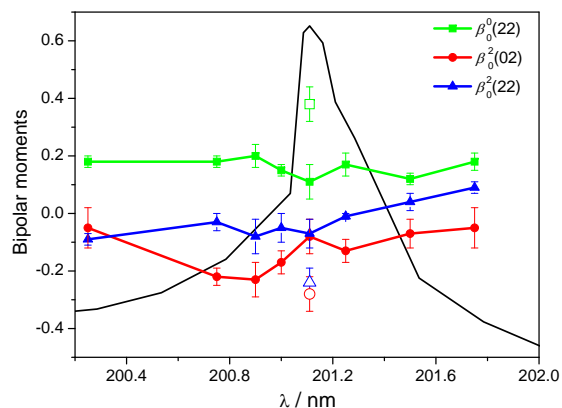
Fig. 11 Variation of the $\beta_0^0(22)$, $\beta_0^2(02)$ and $\beta_0^2(22)$ bipolar moments extracted from the $CH_3(v=0)$ images superimposed to the $CH_3(v=0)$ action spectrum (black line). The open symbols correspond to the corrected bipolar moments once the depolarization factor has been taken into account. The vertical axis scales the bipolar moments, while the action spectrum has been rescaled in arbitrary units to fit in the graph.